

# ANNEALING DEPENDENT MORPHOLOGICAL TRANSITION, CRYSTALLINITY ENHANCEMENT, IR SPECTRA AND OPTICAL PROPERTIES TUNING OF CuO NANOSTRUCTURE SYNTHESIZED BY FACILE PRECIPITATION FOR PHOTOCATALYTIC APPLICATIONS

NOR AZLIA AZIZ, CHAN KOK SHENG\*

Faculty of Science and Marine Environment, University Malaysia Terengganu 21030 Kuala Nerus,  
Terengganu, Malaysia

*E-mails:* ksheng573@gmail.com; chankoksheng@umt.edu.my

\* *Corresponding author:* chankoksheng@umt.edu.my

*Received December 2, 2022*

*Abstract.* In this study, CuO nanostructures were synthesized through facile precipitation route followed by a typical annealing treatment at higher temperature and prolonged time. The SEM analysis revealed that the CuO exhibited various morphological transitions, namely sphere-like, sponge-like, and fiber-like nanostructure depending on the annealing temperature and time. According to the FTIR result, the high-intensity sharp peaks occurred between 500 and 850  $\text{cm}^{-1}$  represent the formation of pure vibrational stretching Cu-O bonds. CuO that underwent annealing treatment at higher temperature and prolonged heating time resulted in finer nanostructure formation, crystallinity improvement, and optical band gap narrowing. These features allow CuO to potentially be used as photocatalyst to degrade the aqueous organic dye pollutants for wastewater remediation applications.

*Key words:* CuO nanostructure, morphological, optical properties.

## 1. INTRODUCTION

Nowadays, metal oxide nanostructures have received tremendous interests and attentions due to their superb semiconducting and optoelectronic properties in many technological applications and device fabrications. Therefore, it is crucial to produce high-quality metal oxides using various chemical and physical techniques, which can provide excellent properties such as good stability and improved compatibility with tunable morphological sizes and optical band gap [1–3]. Interestingly, copper oxide (CuO) is one of the most attractive and vital p-type metal oxide semiconductor materials that possesses a narrow band gap in the range of 1.20–1.80 eV. This band gap value can be adjusted up to 3.5 eV by modifying the morphology and size of CuO nanostructures. CuO also has a wide variety of superior optical, thermal and electrical properties, which can be broadly utilized in the fields of sensors, detectors, energy storage devices, catalysis and other biomedical instruments [4–8].

Many different kinds of CuO morphologies (nanotubes, nanoparticles, nanospheres, nanoflakes, nanosheets and nanorods) can be produced through various physical and chemical synthesis methods, such as sol-gel, sonication, and green mediated, co-precipitation, hydrothermal and microwave-assisted heating methods [9–13]. Among these synthesis routes, facile precipitation is recognized as one of the effective, flexible, fast and environmentally friendly wet chemical techniques. Advantageously, this technique requires only low reaction temperature to precisely control the size and structure of the resulting material, which is also suitable for mass production [7, 11, 13–15]. In this study, the CuO nanostructures were prepared through the precipitation method, followed by thermal annealing at elevated temperature and over a longer period of time. Our purpose is to investigate the evolution occurred in the crystalline structure, optical properties and surface morphology of the CuO samples prepared at different heating temperatures and times. The properties of these materials were then characterized using the instruments such as the SEM, XRD and UV-Vis spectrophotometry.

## 2. MATERIALS AND METHODS

Raw materials used in sample preparation were of analytical grade and used as received without any specific treatment or purification. The precursor materials such as copper (II) sulfate pentahydrate ( $\text{CuSO}_4 \cdot 5\text{H}_2\text{O}$ ) and sodium hydroxide (NaOH) were supplied by Merck Ltd. Firstly, a 0.2 M solution of  $\text{CuSO}_4 \cdot 5\text{H}_2\text{O}$  was prepared, then this solution was heated with continuous stirring until the temperature reached 70°C. At this moment, 1.0 M NaOH was dropwisely added into the solution until the brown precipitate formed at the bottom of the solution, which indicated the formation of CuO. A pH value of 12 was recorded when the precipitate formed. After the solution was cooled to room temperature, the precipitate was collected through filtration. This precipitate was repeatedly rinsed with distilled water several times to remove the impurities, and dried in air for 6 hours. The precipitated powder was then went through the annealing treatment process, *i.e.* the first sample was heated at 100°C for 1 hour (termed as CuO-100T1H), the second one at the same temperature as the first sample but annealed at a longer time, namely 100°C and 6 hours (CuO-100T6H), and the third sample is at the same annealed time compared to the first sample but at a higher temperature, namely 300°C and 1 hour (CuO-300T1H). After annealing, the powders were cooled down to room temperature, and lastly were collected and stored for subsequent material characterizations.

The surface morphology of the as-synthesized CuO samples were characterized by scanning electron microscopy (SEM, JEOL JSM-6390LA) at two different magnifications of  $\times 5000$  dan  $\times 12000$  with an acceleration voltage of 15 kV. The crystallinity and structure of the CuO nanostructures were analyzed from X-ray

diffraction patterns obtained from an X-ray diffractometer (Rigaku Miniflex II), where the scanning range is set between  $2\theta = 10\text{--}80^\circ$  with an  $\text{CuK}_\alpha$  radiation source ( $\lambda = 1.54059$ ). The optical absorbance spectra were recorded using a UV-visible spectrophotometer (Shimadzu, Japan).

### 3. RESULTS AND DISCUSSION

#### 3.1. MORPHOLOGICAL CHARACTERIZATION

SEM micrograph is highly beneficial to determine the shape and size distribution of the nanostructure. The morphological transition of the CuO nanostructure was examined by SEM, in which the images were recorded at lower ( $\times 5,000$ ) and higher ( $\times 12,000$ ) magnification as displayed in Figs. 1a–f. From Figs. 1a,b, it is observed that the CuO–100T1H sample demonstrates a smooth and uniform sphere-like morphology, which is due to the aggregation of many tiny spherical particles to form an interconnected network with small grain size. These nanoparticles are mostly of comparable size and shape, and homogeneously distributed across the sample, which agrees well with the literature [23–25]. This agglomeration can be attributed to the attraction between the adjacent nanoparticles with high surface area through electrostatic force or chemisorption [8]. Moreover, an identical size and shape can also be monitored at higher resolution with a clearer image. As measured from the ImageJ software, the spherical particles have the diameters in the range of 200–350 nm with an average size of 275 nm.

Furthermore, the morphology of CuO with a sponge-like porous texture is obtained for the CuO-100T6H sample as displayed in Fig. 1c,d. Similarly, it can be observed the formation of some slightly aggregated spherical nanoparticles across the sample surface, but accompanied with a uniform dispersion of many nanopores in a compact structure. Hereby, it is worth to note that this sample contains a less regularly hollow structure and the nanoparticles are loosely embedded in a well-order porous framework. Beneficially, such porous and hollow structure can help in capturing more irradiated photons for better light absorption during the photocatalytic reaction activity [25]. Nevertheless, when CuO is heated at elevated temperature up to  $300^\circ\text{C}$  for the CuO-300T1H sample, the SEM images clearly show the formation of a 3D fiber-like nanostructure (Fig. 1e), in which such structure consists of many tiny nanofibers that outgrow from the prevalent center and repeatedly align towards the sample surface (Fig. 1f). This feature is mainly owing to the overgrowth of nanoparticles during nucleation and coalescence process. Moreover, the lengths of these nanofibers are determined to be in the range of around 700–800 nm, with their widths vary from 40 nm to 80 nm. Thus, it is worth to notice that such fine nanofibers possess a high surface area, and would provide more active sites to promote electron transference in an effective

photocatalytic system. Therefore, when comparing these samples, CuO prepared at 300°C deserves the finest morphology with a uniform dispersion of fibers. SEM analysis reveals that the CuO morphology composes of sphere-like, sponge-like, and fiber-like nanostructures. This phenomenon is due to the heterogeneous nucleation that occurs at different annealing times and temperature gradients [12]. The size of nanosphere, the diameter of nanopores, and the width of nanofibers are examined less than 100 nm. These nanostructures contribute to a higher surface area, in which plenty of active sites dispersed over the surface that are useful for photocatalytic reaction.

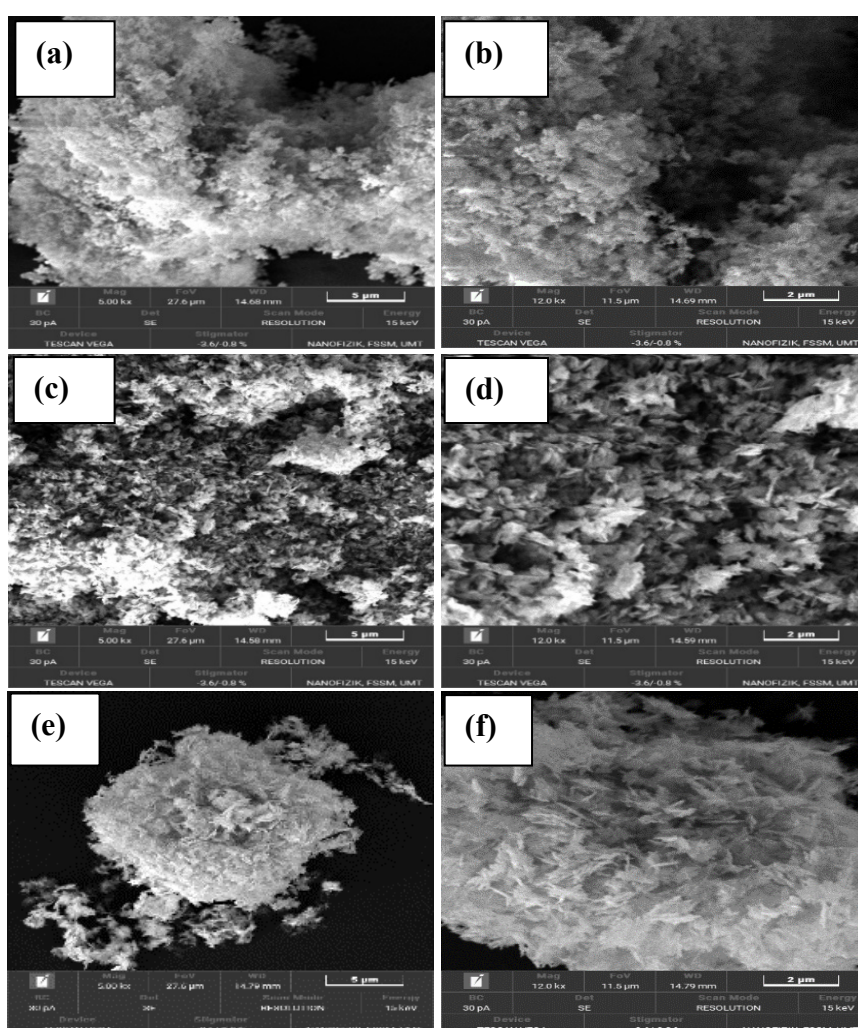


Fig. 1 – SEM micrographs for: (a–b) CuO-100T1H, (c–d) CuO-100T6H, and (e–f) CuO-300T1H samples.

## 3.2. STRUCTURAL ANALYSIS

XRD analysis was performed to identify the crystalline phase and structural properties of the as-synthesized materials. The recorded wide-angle XRD patterns of the present CuO samples are illustrated in Fig. 2. The observed intense diffraction peaks manifest the phase purity and crystallinity nature of the sample. From the figure, the appearance of eleven typical diffraction peaks are traced at  $2\theta$  positions of  $32.42^\circ$ ,  $35.48^\circ$ ,  $38.81^\circ$ ,  $48.80^\circ$ ,  $53.37^\circ$ ,  $58.33^\circ$ ,  $61.47^\circ$ ,  $66.05^\circ$ ,  $68.03^\circ$ ,  $72.42^\circ$  and  $75.01^\circ$ , corresponding to the lattice planes of (1 1 0), (0 0 2), (1 1 1), (-2 0 2), (0 2 0), (2 0 2), (-1 1 3), (-3 1 1), (2 2 0), (3 1 1) and (0 0 4), respectively. These conceivable peak positions agree with the previous literature reports [3, 7, 16–18], and are also well compatible with the standard reference data in JCPDS card # 48–1548 file, hence verifying the monoclinic crystalline phase of CuO (tenorite) with space group  $C2/c$ . By referring to the preferential major peak of the (111) plane, the lattice parameters of  $a$ ,  $b$  and  $c$  that correlated with the monoclinic structure are computed according to the following equation:

$$\frac{1}{d^2} = \frac{1}{\sin^2 \beta} \left( \frac{h^2}{a^2} + \frac{k^2 \sin^2 \beta}{b^2} + \frac{l^2}{c^2} - \frac{2hl \cos \beta}{ac} \right), \quad (1)$$

where  $h$ ,  $k$  and  $l$  are the Miller indices and  $d$  is the lattice spacing, thus the mean lattice parameters obtained for CuO are  $a = 4.69 \text{ \AA}$ ,  $b = 3.42 \text{ \AA}$ ,  $c = 5.14 \text{ \AA}$ ,  $\gamma = 90^\circ$  and  $V = 80.88 \text{ (\AA)}^3$ . Apparently, CuO demonstrates a monoclinic structure, regardless of heating temperature and time. Moreover, it is worth to note that no other extraneous peaks or secondary phases, such like  $(\text{Cu}_2\text{O})$  cuprite or  $\text{Cu}(\text{OH})_2$  was detected in the diffractogram, implying that the samples produced to be of single-phase CuO with high purity. The predominant diffraction peak intensities along the (002) and (111) lattice planes indicate that the preferential orientations of most crystallites are in these plane directions. However, the peak intensity of the (111) plane is slightly higher than the (002) plane, unless for the CuO-300T1H sample, since the intensities of both planes are close to each other. On the other hand, the peak intensity shows a significant enhancement accompanied by a slight reduction in peak width as the annealing temperature and duration increase. This phenomenon indicates that the crystallinity of the samples relies significantly on the annealing condition. Moreover, the peak narrowing can be ascribed to a small increment in the crystallite size, where higher annealing temperature and time facilitate the growth of larger crystallite size. Commonly, X-rays diffract on multiple planes when the crystallite size is extremely small with non-uniform applied strain, which in turn induces the peak broadening [2, 5, 19, 20].

Subsequently, the average crystallite size of the CuO photocatalyst is ascertained from the peak width *via* the Debye-Scherrer relation:  $D = 0.9 \lambda / \beta \cos \theta$ ,

where:  $D$  is the average crystallite size,  $\lambda$  denotes the X-ray wavelength of Cu  $K\alpha$  radiation,  $\beta$  is the full width at half maximum (FWHM) of each XRD peak in radians and  $\theta$  represents the Bragg's diffraction peak angle. As computed from the Scherer's equation, the average crystallite size for CuO-100T1H (sphere-like structure), CuO-100T6H (sponge-like structure) and CuO-300T1H (fiber-like structure) is found to be  $\sim 13.53$  nm, 13.95 nm and 14.84 nm, respectively. The crystallite size exhibits a slight increment with the raise of annealing duration and temperature, indicating the growth of larger crystallite size due to a strong interaction between the molecules with higher surface energy. This result is in accordance with the one reported in the literature [21–23]. On the other hand, the mean dislocation density ( $\delta$ ) that represents the number of defects in the material, as defined by the length of dislocation lines per unit volume of crystal is given by the following formula:  $\delta = 1/D^2$ . The micro strain as well as the crystallite size mainly relies on the width of diffraction peak, and therefore according to Williamson-Hall model, the micro strain ( $\epsilon$ ) values are determined using the equation:  $\epsilon = (\beta / 4\tan\theta)$ . The structural parameters of the crystallite size ( $D$ ), micro strain ( $\epsilon$ ) and dislocation density ( $\delta$ ) for the present samples are summarized in Table 1. From the results, it is worth to note that the micro strain and dislocation density show an inverse relationship with the crystallite size. This feature is in line with the previous work reported by George *et al.* [2]. Conclusively, the CuO monoclinic structure is preserved after annealing at higher temperature and prolonged time. Therefore, the production of CuO with high crystallinity could be intentionally controlled to meet the desirable applications for optoelectronics and photocatalytic activity.

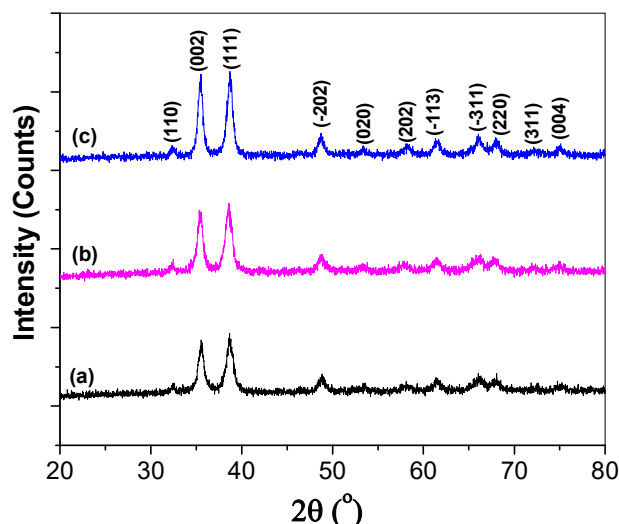


Fig. 2— XRD patterns of the CuO samples for: a) CuO-100T1H; b) CuO-100T6H; c) CuO-300T1H.

Table 1

The structural parameters determined for the present CuO samples

Samples	Average crystallite size, $D$ [nm]	Micro strain, $\varepsilon$ [ $\times 10^{-3}$ ]	Dislocation density, $\delta$ [ $\times 10^{-3} \text{ nm}^{-2}$ ]
CuO-100T1H	13.53	8.789	5.4627
CuO-100T6H	13.95	8.547	5.1387
CuO-300T6H	14.84	8.005	4.5408

### 3.3. OPTICAL PROPERTIES

The absorbance spectra were recorded using the UV-Vis spectrophotometer in order to elucidate the optical properties of the present samples under visible light irradiation. Principally, the absorbance is owing to the transition of electrons between the valence and conduction bands stimulated by instantaneous photonic excitation. The absorption spectra of the present CuO samples were recorded in the wavelength region between 300 nm and 800 nm as displayed in Fig. 3. After the synthesis, the colorless mixture of the aqueous precursors was changed into a brownish-black precipitated solution. As a consequence, a well-defined broad absorption band centered at 441 nm is observed in the visible spectral region. This feature implies the existence of a fine CuO nanostructure that are preferable for visible light absorption, which is also in accordance with the recently reported literature [9, 20–26]. Meanwhile, the absorbance intensity shows a gradual decay beyond 500 nm irradiation. The sample annealed at higher temperature or prolonged duration demonstrates a stronger absorption intensity than the others. This effect is attributed to a smaller structure produced with a larger surface area to volume ratio that is consistent with the SEM image analysis. Therefore, the increase in absorption suggests that CuO can be employed as a good absorbing material for solar cell application and also for photocatalytic degradation activity [8, 27, 28]. On the other hand, the observed clear and linear absorbance edge dictates a good crystallinity of CuO nanostructure, as also supported by XRD analysis [13]. The band gap energy,  $E_g$  is determined from the absorbance spectrum using the Tauc's direct optical transition, which is represented by the formula as follows:

$$(\alpha h\nu) = B (h\nu - E_g)^{1/2}, \quad (2)$$

where  $\alpha$  represents the absorption coefficient ( $\text{cm}^{-1}$ ),  $B$  is a constant,  $h$  denotes the Planck's constant ( $h = 6.626 \times 10^{-34} \text{ Js}$ ),  $\nu$  is the frequency of light irradiation,  $h\nu$  is the photon energy, and  $E_g$  is the band gap energy [3, 29, 30]. Also, the Beer-Lambert law defines the absorption coefficient ( $\alpha$ ) is directly proportional to the absorbance. Figure 3 also shows the Tauc's plot of  $(\alpha h\nu)^2$  as a function of photon

energy. The band gap energy can be determined by extrapolating the linear portion of the curve to intersect at a point of the photon energy ( $h\nu$ ) axis. The determined band gap energy values of the CuO samples lie in the range of (1.63–1.67) eV that agrees well with Peng *et al.* [31] and Pavithra *et al.* [32]. Furthermore, these values obtained are much higher than those of the reported band gap of bulk CuO (1.2–1.5 eV) [13, 33–35], which can be associated with quantum confinement effect due to the formation of the nanostructured materials with smaller crystallite size and specified morphology [2, 10, 16, 20, 36]. Nevertheless, the band gap shows a slight reduction or so-called blue shift when the CuO is annealed at higher annealing temperature or longer duration. This tunable effect is mainly attributed to the alteration in shape, grain size and crystallinity of the CuO nanostructures at different preparation conditions [31, 37–40]. Meanwhile, smaller band gap might improve the photocatalyst efficiency due to enhanced charge carrier transfer and separation [39].

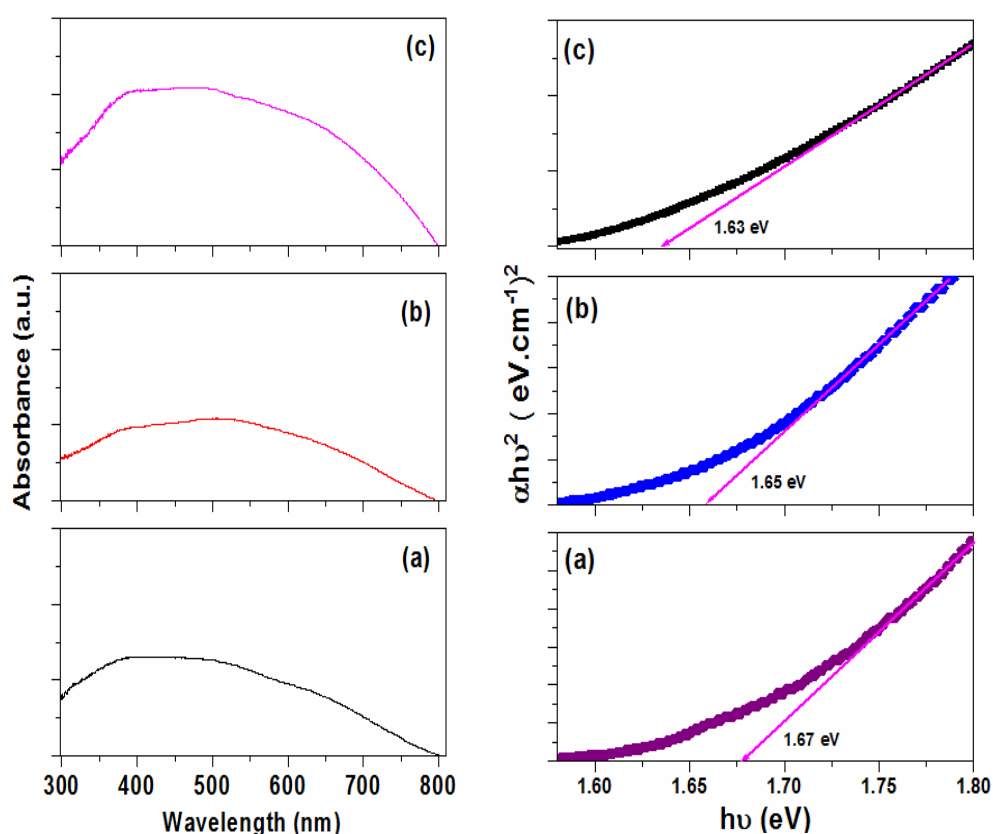


Fig. 3 – UV-vis absorbance spectra (left) and the Tauc's plot (right) of CuO nanostructures for: a) CuO-100T1H; b) CuO-100T6H; c) CuO-300T1H samples.

## 3.4. FUNCTIONAL GROUPS

The FTIR analysis was performed in order to prevail the possible vibrational modes and functional groups present on the surface of the as-synthesized CuO. Figure 4 depicts the FTIR profile of the present CuO recorded in the 400–4000  $\text{cm}^{-1}$  wavenumber range. From the spectra, a broad and intense band observed near 3389  $\text{cm}^{-1}$  and another peak situated at 1639  $\text{cm}^{-1}$  are attributed to the stretching and bending vibrational modes of the hydroxyl (O–H) groups, respectively [18, 19]. This result is due to the atmospheric water molecules that adsorbed on the CuO sample surface [41–43], since the nanostructured materials are keen to absorb high amounts of moisture content and gas molecules because of their large surface area to volume ratio. Meanwhile, the intense IR peaks positioned at 515  $\text{cm}^{-1}$ , 608  $\text{cm}^{-1}$ , 678  $\text{cm}^{-1}$  and 842  $\text{cm}^{-1}$  mainly correspond to the vibrational stretching of Cu–O bond, thereby further confirming the formation of a pure CuO. This result is in a well accordance with the previous studies [11, 20, 21], in which the relative significant bands found around 600–1000  $\text{cm}^{-1}$  region represent the metal oxide compounds. Nevertheless, the prominent sharp peak appeared at 2358  $\text{cm}^{-1}$  corresponds to the  $\text{CO}_2$  gas molecules that adsorbed on the sample surface during and after the synthesis process [22].

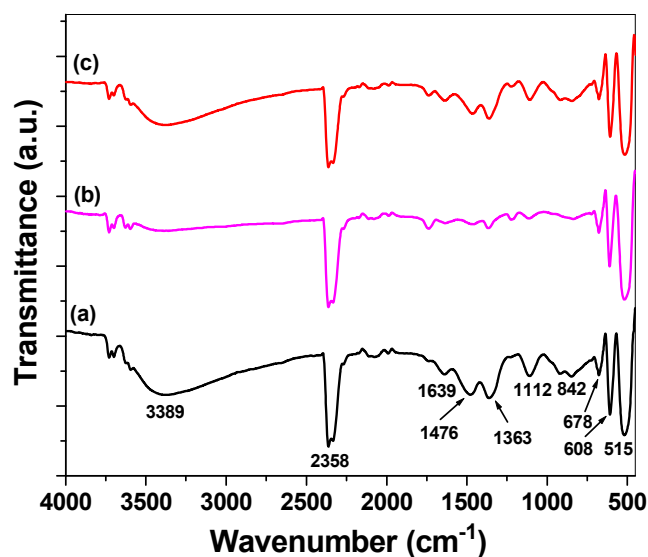


Fig. 4 – FTIR spectrum for: a) CuO-100T1H; b) CuO-100T6H; c) CuO-300T1H.

In addition, another minor peak observed at 1476  $\text{cm}^{-1}$  might be ascribed to the presence of an asymmetric carbonyl C=C stretching band [21], whereas a small band that emerged at 1112  $\text{cm}^{-1}$  is due to C=O stretching vibration [23]. These peaks remain strong at higher annealing temperature as observed for CuO-300T1H

sample. Moreover, a small peak located at  $1363\text{ cm}^{-1}$  is likely to be assigned to the alkoxy -C-O- stretching bonds [24]. Interestingly, the band at  $3389\text{ cm}^{-1}$  becomes negligible, and those peaks at  $1112\text{ cm}^{-1}$ ,  $1363\text{ cm}^{-1}$ ,  $1639\text{ cm}^{-1}$  and  $1476\text{ cm}^{-1}$  diminish when CuO annealed at prolonged duration. This phenomenon implies the detachment of the related compounds or gas molecules from the sample surface. As for comparison, the samples annealed at elevated temperature up to  $300^\circ\text{C}$  show only a slight decrease in peak intensity for all the functional groups attached to the sample surface, except the respective peaks that represent Cu-O, where this substance remains dominant after annealing treatment.

#### 4. CONCLUSION

In summary, we have successfully fabricated the CuO nanostructure *via* facile precipitation and underwent thermal annealing treatment at higher temperature and longer time. SEM results show that CuO demonstrates various morphologies, namely sphere-like, sponge-like, and fiber-like nanostructures, where the fiber-like structure being the finest, as for the sample annealed at higher temperature of  $300^\circ\text{C}$ . XRD analysis shows that the crystallinity of CuO improves as the annealing temperature and time increase. From the optical absorbance spectra, CuO shows a good absorption indicated by the main peak located at  $441\text{ nm}$ . The optical band gap that was determined from Tauc's plot demonstrates a slight decrease when the temperature and heating time increase, which allows the photo-induced charge carrier transition becomes much easier for the photocatalytic activity.

*Acknowledgements.* The authors gratefully acknowledge the University Malaysia Terengganu and the Malaysian Government for this work's technical and financial support through the research grant (TAPE-RG-55290).

#### REFERENCES

1. Q. Zhou, Y. Zhang, T. Zeng, Q. Wan and N. Yang, *Anal. Chim. Acta* **1171**, 338663 (2021).
2. A. George, D. M. A. Raj, X. Venci, A. D. Raj, A. A. Irudayaraj, R. L. Josephine, S. J. Sundaram, A. M. Al-Mohaimed, D. A. A. Farraj, T. Chen and K. Kaviyarasu, *Environ. Res.* **203**, 111880 (2022).
3. A. Ahmad, M. Khan, S. Khan, R. Luque, K. M. Abualnaja and O. K. Alduaij, T. A. Yousef, J. *Mol. Struct.* **1256**, 132522 (2022).
4. A. George, D. M. A. Raj, A. D. Raj, B. Nguyen, T. Phan, T. Pazhanivel, K. Sivashanmugan, R. L. Josephine, A. A. Irudayaraj, J. Arumugam and V. Nguyen, *Mater. Lett.* **281**, 128603 (2020).
5. M. E. Bustos, F. Hevia, S. Fuentes, A. I. Martínez and R. A. Zárate, *Mater. Lett.* **297**, 129936 (2021).
6. Z. Yang, Q. Rong, T. Bao, M. Jiao, L. Mao, X. Xue, W. Wen, Z. Wu, X. Zhang and S. Wang, *Anal. Chim. Acta* **1199**, 339598 (2022).
7. A. K. Sibhatu, G. K. Weldegebrical, S. Sagadevan, N. N. Tran and V. Hessel, *Chemosphere* **300**, 134623 (2022).
8. K. Alsamhary, N. M. Al-Enazi, E. Alhomaidi and S. Alwakeel, *Environ. Res.* **207**, 112172 (2022).
9. H. J. Prabu, R. Varghese, I. Johnson, S. J. Sundaram, A. D. Raj, R. Rajagopal, P. Kuppasamy, R. Sathya and K. Kaviyarasu, *Environ. Res.* **212**, 113295 (2022).

10. A. P. M. Udayan and S. N. Sawant, *J. Phys. Chem. Solids* **150**, 109883 (2021).
11. N. A. S. K. Anuar and C. K. Sheng, *J. Nano-Electron. Phys.* **13**, 05015 (2021).
12. U. Nakate, Y. Yu and S. Park, *Microelectron. Eng.* **251**, 111662 (2022).
13. Z. R. Parekh, S. H. Chaki, A. B. Hirpara, G. H. Patel, R. M. Kannaujiya, A. J. Khimani and M. P. Deshpande, *Physica B Condens. Matter.* **610**, 412950 (2021).
14. C. K. Sheng and Y. M. Alrababah, *Kuwait J. Sci.* **49**, 1–10 (2022).
15. C. K. Sheng and Y. M. Alrababah, *J. Nano- Electron. Phys.* **12**, 01017 (2020).
16. T. Gudipati, M. B. Zaman, P. Singh and R. Poola, *Inorg. Chem. Commun.* **130**, 108677 (2021).
17. N. S. Pavithra, K. N. Manukumar, R. Viswanatha and G. Nagaraju, *Inorg. Chem. Commun.* **130**, 108689 (2021).
18. Y. M. Alrababah, C. K. Sheng and M. F. Hassan, *Nano-Struct. & Nano-Objects* **19**, 10034 (2019).
19. K. S. Chan and W. M. M. Yunus, *Pertanika J. Sci. Technol.* **13**, 23–30 (2005).
20. A. George, D. M. A. Raj, A. D. Raj, A. A. Irudayaraj, J. Arumugam, M. S. kumar, H. J. Prabu, S. J. Sundaram, N. A. Al-Dhabi, M. V. Arasu, M. Maaza and K. Kaviyarasu, *Surf. Interfaces* **21**, 100761 (2020).
21. A. G. Raju, B. D. Rao, G. Himabindu and S. M. Botsa, *J. Mater. Res. Technol.* **17**, 2648–2656 (2022).
22. M. An, L. Li, X. Gao, Y. Zhu, J. Guan and Q. Wu, *Colloids Surf. A: Physicochem. Eng. Asp.* **643**, 128794 (2022).
23. N. S. Pavithra, K. N. Manukumar, R. Viswanatha and G. Nagaraju, *Inorg. Chem. Commun.* **130**, 108689 (2021).
24. D. Das and P. Nandi, *Appl. Surf. Sci.* **570**, 151260 (2021).
25. Q. Qin, N. Qiao, Y. Liu and X. Wu, *Appl. Surf. Sci.* **521**, 146479 (2020).
26. G. Wang, Y. Zhang, L. Ge, Z. Liu, X. Zhu, S. Yang, P. Jin, X. Zeng and X. Zhang, *J. Hazard. Mater.* **429**, 128282 (2022).
27. G. Sabena, S. Rajadurai, E. Pushpalakshmi, H. A. Alhadlaq, R. Mohan, G. Annadurai and A. Maqsood, *J. King Saud Univ. Sci.* **34**, 102092 (2022).
28. K. Sahu, B. Satpati and S. Mohapatra, *Ceram. Int.* **46**, 24407–24412 (2020).
29. C. K. Sheng, K. A. M. Amin, L. L. Hong, M. F. Hassan and M. Ismail, *Int. J. Electrochem. Sci.* **12**, 10023–10031 (2017).
30. Y. M. Alrababah, C. K. Sheng and M. F. Hassan, *Chalcogenide Lett.* **16**, 297–301 (2019).
31. W. Peng, Y. Zhou, J. Li, Y. Liu, J. Zhang, G. Xiang, X. Zhu, R. Li, H. Wang and Y. Zhao, *Mater. Sci. Semicond. Process.* **131**, 105883 (2021).
32. N.S. Pavithra, K.N. Manukumar, R. Viswanatha and G. Nagaraju, *Inorg. Chem. Commun.* **130**, 108689(2021).
33. S. Kulkarni and R. Ghosh, *Sens. Actuators B Chem.* **335**, 129701 (2021).
34. A. Ghosha, M. Miahb, A. Beraa, S. K. Sahab and B. Ghosha, *J. Alloys Compd.* **862**, 158549 (2021).
35. H. Absike, Z. Essalhi, H. Labrim, B. Hartiti, N. Baaalla, M. Tahiri, B. Jaber and H. Ez-Zahraouy, *Opt. Mater.* **118**, 111224 (2021).
36. J. Uddin, M. Sharmin, M. N. Hasan and J. Podder, *Opt. Mater.* **119**, 111388 (2021).
37. S. Sharma, K. Kumar, N. Thakur, S. Chauhan and M. S. Chauhan, *J. Environ. Chem. Eng.* **9**, 105395 (2021).
38. B. Uma, K.S. Anantharaju, L. Renuka, S. Malini, S. S. More, Y.S. Vidya and S. Meena, *Ceram. Int.* **47**, 10355–10369 (2021).
39. M. F. A. Aziz, N. L. A. Wahab and K. S. Chan, *Mal. J. Microsc.* **7**, 109–115 (2011).
40. W. M. M. Yunus, K. S. Chan and W. M. Z. W. Yunus, *J. Nonlinear Opt. Phys. Mater.* **12**, 91–100 (2003).
41. M.F. Hassan, S.K. Zainuddin, K. H. Kamarudin, C. K. Sheng, M. A. A. Abdullah, *Malaysian J. Anal. Sci.* **22**, 238-248 (2018).
42. M.F.A. Aziz, N. L. A. Wahab, K. S. Chan, *Mal. J. Microsc.* **7**, 109-115 (2011).
43. C. K. Sheng, W. M. M. Yunus, W. M. Z. W. Yunus, M. Z. A. Rahman, *Mater. Phys. Mech.* **48**, 1–8 (2022).